JACS
JOURNAL OF THE AMERICAN CHEMICAL SOCIETY
pubs.acs.org/JACS
Article

Structural Disorder in Higher-Temperature Phases Increases Charge Carrier Lifetimes in Metal Halide Perovskites

Ran Shi, Qiu Fang, Andrey S. Vasenko, Run Long,* Wei-Hai Fang, and Oleg V. Prezhdo

Cite This: J. Am. Chem. Soc. 2022, 144, 19137−19149
Read Online
ACCESS | Metrics & More | Article Recommendations | Supporting Information

ABSTRACT: Solar cells and optoelectronic devices are exposed to heat that degrades performance. Therefore, elucidating temperature-dependent charge carrier dynamics is essential for device optimization. Charge carrier lifetimes decrease with temperature in conventional semiconductors. The opposite, anomalous trend is observed in some experiments performed with $MAPbI_3$ (MA = $CH_3NH_3^+$) and other metal halide perovskites. Using ab initio quantum dynamics simulation, we establish the atomic mechanisms responsible for nonradiative electron−hole recombination in orthorhombic-, tetragonal-, and cubic $MAPbI_3$. We demonstrate that structural disorder arising from the phase transitions is as important as the disorder due to heating in the same phase. The carrier lifetimes grow both with increasing temperature in the same phase and upon transition to the higher-temperature phases. The increased lifetime is rationalized by structural disorder that induces partial charge localization, decreases nonadiabatic coupling, and shortens quantum coherence. Inelastic and elastic electron−vibrational interactions exhibit opposite dependence on temperature and phase. The partial disorder and localization arise from thermal motions of both the inorganic lattice and the organic cations and depend significantly on the phase. The structural deformations induced by thermal fluctuations and phase transitions are on the same order as deformations induced by defects, and hence, thermal disorder plays a very important role. Since charge localization increases carrier lifetimes but inhibits transport, an optimal regime maximizing carrier diffusion can be designed, depending on phase, temperature, material morphology, and device architecture. The atomistic mechanisms responsible for the enhanced carrier lifetimes at elevated temperatures provide guidelines for the design of improved solar energy and optoelectronic materials.

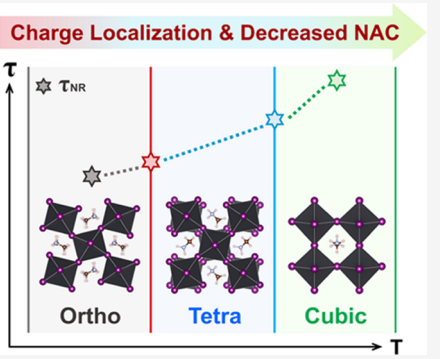

1. INTRODUCTION

Hybrid organic−inorganic halide perovskites (HOIPs) have been identified recently as appealing photovoltaic materials due to their low-cost fabrication and excellent optoelectronic properties, including direct and tunable band gap,[1,2] high defect tolerance,[3,4] strong light absorption,[5] long carrier diffusion,[6,7] low exciton binding energies,[8] and long excited-state lifetimes.[6,9] These characteristics promote the application of HOIPs to a variety of fields and devices,[10−17] such as photodetectors,[10,11] light-emitting diodes,[12,13] field effect transistors,[14] lasers,[15] and solar cells.[16,17] Performance of HOIP solar cells has witnessed significant breakthroughs with the record power conversion efficiency growing rapidly from 3.81[18] to 25.7%[19] within a dozen years. Poor stability[20,21] of perovskite solar cells (PSCs) has become the main barrier for large-scale commercialization.

The challenges posed by harsh operating conditions of PSCs, such as exposure to solar radiation,[22] oxygen, and moisture,[23] can be addressed by encapsulation techniques.[24,25] However, significant variations in temperature, ranging from 250 to 310 K,[26,27] and sometimes exceeding 340 K,[26] are unavoidable. Therefore, systematic studies should be carried out over a wide temperature range, to maintain and improve the advanced photoconversion features. Since nonradiative electron−hole recombination is the main pathway for charge and energy losses in PSCs, the carrier recombination time is a good indicator characterizing the PSC efficiency.[21,28,29] Establishing the influence of thermal effects on the charge carrier dynamics of perovskites is of much significance to the scientific and engineering communities.

A typical HOIP, methylammonium lead iodide ($MAPbI_3$, MA = $CH_3NH_3^+$) is composed of a three-dimensional inorganic backbone formed by corner sharing PbI_6 octahedra, and the organic $CH_3NH_3^+$ cations filling in the cavities and interacting with the octahedra through hydrogen bonding.[30−32] The cations exhibit relatively long-range electrostatic order, which decreases with increasing temperature. The cations migrate toward the cavity centers, changing the hydrogen-bonding interaction with the inorganic backbone. This process contributes to the deformation of the PbI_3 framework, leading

Received: August 13, 2022
Published: October 7, 2022

https://doi.org/10.1021/jacs.2c08627
J. Am. Chem. Soc. 2022, 144, 19137−19149

to structural phase transitions. The low-temperature orthorhombic phase transforms into the intermediate tetragonal phase and high-temperature cubic phase.[33,34] The early studies of the temperature dependence have focused on the fundamental band gap of $MAPbI_3$,[35−38] which exhibits an unusual positive correlation with temperature. The trend is in contrast to the conventional semiconductors, in which the band gap decreases as temperature increases.[39] Subsequent temperature-dependent photo-physics studies of HOIPs uncovered other interesting phenomena,[40−43] including transformation of charges between exciton and free carrier states,[44−47] order−disorder transitions due to rotation of the organic cations,[48,49] and unusual atomic mechanisms of formation of polarons and trap states.[50−55] Subsequent works investigated temperature-dependent charge carrier dynamics,[34,56] including charge transfer,[42,44] intraband relaxation,[57−59] and electron−hole recombination.[60−62]

Wehrenfennig et al. studied the influence of the low-temperature evolution, associated with the tetragonal-to-orthorhombic phase transition, on the charge carrier recombination in the $MAPbI_{3-x}Cl_x$ perovskite, and demonstrated faster recombination at the lower temperature.[61] Applying optical-pump terahertz-probe photoconductivity spectroscopy, Johnston and co-workers investigated the high-temperature evolution, exhibiting the tetragonal-to-cubic phase transition, and came to a similar conclusion: the charge recombination was suppressed with increasing temperature.[63] The result was confirmed by Milot et al. and Trimpl et al. for the $MAPbI_3$ perovskite.[60,62] However, Grozema's group held a contrary opinion that the bi-molecular charge recombination rate increased with temperature.[64] They attributed the long lifetime in the orthorhombic phase to the enhanced charge separation due to increased ordering of the organic cations at low-temperature. Munson proposed that charge carrier localization could reduce mobility but extend lifetime owing to the dynamic disorder at higher temperatures.[65] Such interplay has important implications for solar cells, whose efficiency is most directly related to the carrier diffusion length that requires both large mobility and lifetime. Working solar cells are sensitive to temperature variation,[62] and therefore, it is necessary to understand the mechanisms of temperature-dependent charge carrier recombination. This goal can be achieved via atomistic quantum dynamics simulations. The prior simulations focused on the tetragonal phase of $MAPbI_3$.[66−68] Since most measurements are performed around phase-transition temperatures, and because there exist three stable phases of the $MAPbI_3$ perovskite, it is important to investigate how the charge carrier lifetimes depend on the phase.

Stimulated by the recent experimental reports,[34,60−63] we use real-time time-dependent density functional theory[69,70] (TDDFT) and nonadiabatic (NA) molecular dynamics[71−78] (MD) to model systematically the nonradiative electron−hole recombination process in orthorhombic-, tetragonal-, and cubic-phase $MAPbI_3$ at the phase-transition temperatures.[34] The calculations demonstrate that the changes in the structural order arising from the phase transitions are as important as those arising from heating of the same phase and that inelastic and elastic electron−vibrational interactions show opposite dependence on both temperature and phase. Thermal motions of light MA organic cations become disordered upon heating from 162 to 315 K, enhancing the deformation of the $[PbI_6]^{4-}$ inorganic backbone through hydrogen bonding and steric interactions. The enhanced thermal fluctuations at higher temperatures activate high-frequency vibrations, accelerate quantum coherence loss, and slow down nonradiative charge recombination, according to the quantum Zeno effect.[79] The reduction of the I−Pb−I angle with temperature decreases the overlap between the Pb and I atomic orbitals, which compose the band-edge states, and opens up the band gap. The Pb−I inorganic lattice distortion gives rise to localized and separated charge densities, minimizing the overlap of conduction band electron and valence band hole, and decreasing the NA coupling by more than 40%. All of the above factors prolong the excited-state lifetime. The simulations rationalize the abnormal phase and temperature dependence of charge recombination in the $MAPbI_3$ perovskite, emphasize the influence of phase and temperature on charge localization, and provide useful insights for control of operating conditions of solar energy and optoelectronic devices.

2. METHODS

The ab initio NAMD simulations are performed using the decoherence-induced surface hopping (DISH)[80] technique implemented within TDDFT in the Kohn−Sham (KS) framework.[69,70] Within the mixed quantum-classical dynamics approach, the lighter and faster electrons are treated quantum mechanically, and the heavier and slower nuclei are modeled semiclassically.[81,82] The destruction of superpositions formed between pairs of electronic states via NA coupling is regarded as decoherence.[80,82] The decoherence time is evaluated as the pure-dephasing time using the optical response theory.[83−86] Quantum transitions appear in the DISH algorithm as a result of the decoherence process and occur at decoherence effects, which provide the physical basis for hops.[82] The method has been applied to study photoexcitation dynamics in a broad range of materials, including black phosphorus,[87,88] transition-metal dichalcogenides,[89−93] two-dimensional (2D) Ruddlesden−Popper and Dion−Jacobson perovskites,[94,95] lead halide perovskites containing dopants,[96,97] defects,[21,28,98,99] isotopes,[100] grain boundaries, and edge states,[101−103] interacting with water or oxygen molecules,[101,104,105] responding to strain and thermal effects,[67,106,107] etc.[108−112]

The geometry optimization and adiabatic MD are carried out using the Vienna ab Initio Simulation Package (VASP).[113] The Perdew−Burke−Ernzerhof functional is used to describe electronic exchange−correlation interactions,[114] and the projector-augmented wave (PAW) approach is used to treat electron−ion interactions.[115] The plane wave energy cutoff is set to 400 eV. For the geometry optimization, a $2 \times 2 \times 2$ Monkhorst−Pack k-point mesh is adopted for the orthorhombic and tetragonal $MAPbI_3$ systems, and $2 \times 1 \times 1$ for the cubic $MAPbI_3$ system. For the density of states (DOS) calculations, a much denser $4 \times 4 \times 3$ Monkhorst−Pack k-point mesh is adopted for all systems. All systems contain the same number of atoms, 384, in each supercell. The geometry optimization stops when the ion forces are less than 10^{-3} eV/Å. The van der Waals interactions are described using the Grimme DFT-D3 method with the Becke−Johnson damping.[116,117]

The NA coupling calculations[118,119] and NAMD simulations of the nonradiative electron−hole recombination are performed at the Γ-point for the orthorhombic and tetragonal phases, and the R-point for the cubic phase, since the three studied phases are direct band gap materials with the conduction band minimum (CBM) and valence band maximum (VBM) located at these k-points. After the geometry optimization, repeated velocity rescaling is applied for 2 ps to heat the systems to the temperatures of the phase transitions. In particular, the orthorhombic and tetragonal phases are heated to 162 K, and the tetragonal and cubic phases to 315 K. Then, 6 ps adiabatic MD trajectories are generated in the microcanonical ensemble with a 1 fs atomic time step. The 6 ps length of the trajectories is selected based on the need to sample properly atom motions present in $MAPbI_3$, and is limited by the expense of ab initio simulations. The slowest relevant motion is rotation of MA cations, which occurs on a timescale of a few

https://doi.org/10.1021/jacs.2c08627
J. Am. Chem. Soc. 2022, 144, 19137−19149

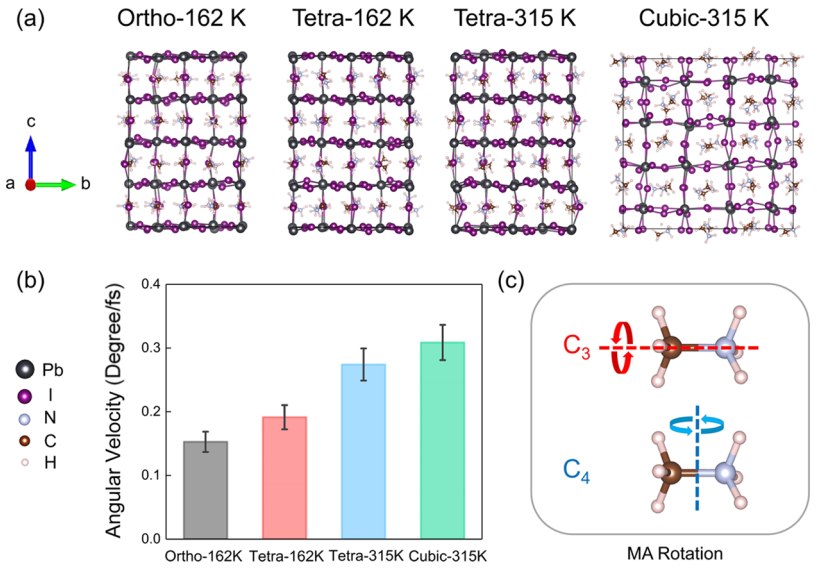

Figure 1. (a) Representative geometries of $MAPbI_3$ for the Ortho-162 K, Tetra-162 K, Tetra-315 K, and Cubic-315 K phases. (b) Average angular velocity of MA cations along the 6 ps MD trajectories. The error bars characterize the variation of the MA rotation. (c) Schematic of MA rotations along the C_3 and C_4 axes. The C_3 notation stems from the symmetry of the MA cation, while C_4 is defined by the cubic symmetry of the inorganic lattice. Thermal rotations and fluctuations of the MA cations have an indirect but important influence on electron−hole and electron−vibrational interactions.

picoseconds, and can be sampled by the 6 ps trajectories. To study the electron−hole recombination process, The NA Hamiltonian obtained during the 6 ps trajectory is iterated multiple times to obtain the nanosecond charge recombination dynamics. The first 3000 geometries from the adiabatic MD trajectories are chosen as initial configurations for the NAMD simulations, which are performed using the PYXAID code.[81,82] This approach has generated reliable and important insights into quantum dynamics of charge carriers in metal halide perovskites[21,28,67,94−107] and many other materials.[87−93,108−112] It provides a compromise between computational efficiency and the need to model nanosecond charge recombination timescales, which cannot be achieved yet by direct ab initio quantum dynamics simulation.

3. RESULTS AND DISCUSSION

3.1. Geometric Structure and Thermal Fluctuations.

$MAPbI_3$ is known to exist in the orthorhombic phase (space group *Pnma*) below 162 K, the tetragonal phase (space group *I4/mcm*) at temperatures between 162 and 315 K, and the cubic phase (space group $Pm\bar{3}m$) above 315 K.[33,34] The optimized lattice constants of the three-phase $MAPbI_3$ systems are summarized in Table S1, agreeing well with the experimental and theoretical values.[120,121] To investigate systematically the geometric and electronic structure, electron−vibrational interactions, and charge recombination dynamics in the three $MAPbI_3$ phases, we construct the three model systems to contain the same number of atoms. Namely, we build a $(2 \times 2 \times 2)$ supercell for the orthorhombic and tetragonal phases, and a $(2 \times 4 \times 4)$ supercell for the cubic phase. The systems for each phase contain 32 formula units ($MA_{32}Pb_{32}I_{96}$). Then, we compare the properties of the phase pairs at their corresponding phase-transition temperatures.[34] That is, we study the orthorhombic and tetragonal $MAPbI_3$ systems at 162 K and the tetragonal and cubic $MAPbI_3$ systems at 315 K.

Figure 1a shows the $MAPbI_3$ simulation cells of the orthorhombic phase heated to 162 K (denoted as Ortho-162 K), the tetragonal phase heated to 162 K (Tetra-162 K), the tetragonal phase heated to 315 K (Tetra-315 K) and the cubic phase heated to 315 K (Cubic-315 K). Since metal halide perovskites are soft, compared to the traditional inorganic semiconductors such as Si, TiO_2, and CdSe, thermal fluctuations are significant with anharmonicity having a strong impact on electron−hole and charge−phonon interactions.[68,118] The MA cation rotation varies from completely frozen to facile reorientation with increasing temperature,[33] influencing the geometry and dynamics,[122,123] and playing a major role in ferroelectricity,[124,125] polaron formation,[52] and charge transport and recombination.[57,62] Most MA cations are aligned toward the distorted faces of the PbI_3 cage with certain orientations preferred in the low-temperature orthorhombic and tetragonal phases (Figure 1a).[33] The MA rotations become more disordered and isotropic in the high-temperature cubic phase. To quantitatively characterize the rotation of the MA cations, we calculated their average angular velocity along the 6 ps MD trajectories for each system (Figure 1b), with the standard deviations shown by the error bars. The average angular velocity of the MA rotation increases in the order: Ortho-162 K (0.153°/fs) < Tetra-162 K (0.191°/fs) < Tetra-315 K (0.274°/fs) < Cubic-315 K (0.309°/fs). The standard deviation also follows the same order. The larger angular velocity at higher temperatures can be attributed to the higher kinetic energy. However, the differences between the systems at the same temperature stem from the structural properties of each phase. The rotation along the C−N bond of the MA cation has the C_3 symmetry (Figure 1c) and is allowed in all phases. In contrast, the rotations perpendicular to the C−N bond depend on the inorganic lattice. Based on the symmetry of the cubic phase, this rotation can be labeled as C_4. While this rotation is allowed in the more symmetric, higher-temperature cubic and tetragonal phases, it is strongly hindered in the lower-temperature orthorhombic phase.[126] Comparison of the MA rotations of the different phases at the same temperature indicates that the phase with the larger cavity allows faster rotation, i.e., cubic faster than tetragonal at 315 K, and tetragonal faster than orthorhombic at 162 K. The thermally

https://doi.org/10.1021/jacs.2c08627
J. Am. Chem. Soc. 2022, 144, 19137−19149

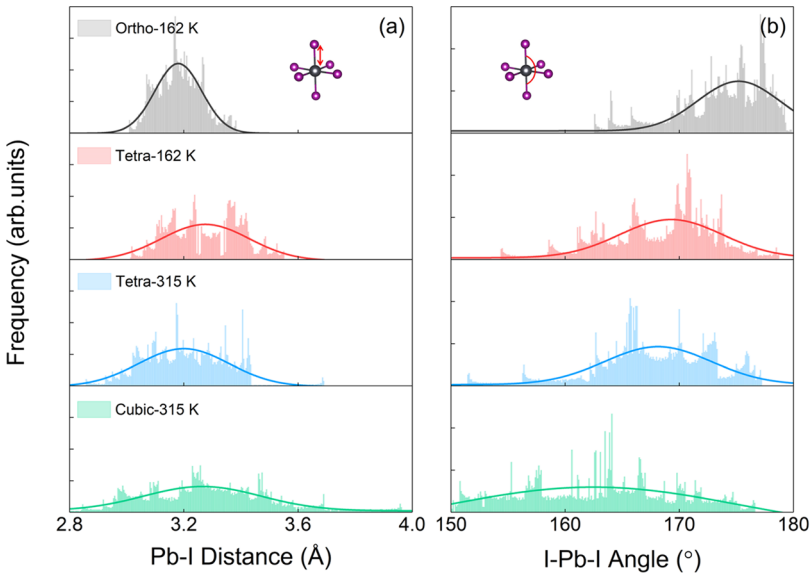

Figure 2. Histograms of (a) Pb−I bond distances and (b) I−Pb−I bond angles, illustrated in the inserts, computed over the MD trajectories at 162 and 315 K for the four systems under investigation. As temperature is increased, the distributions broaden and shift. The bonds become longer, while the angles decrease. Considering the phase pairs at the phase-transition temperatures, the higher-temperature phases are more disordered than the lower-temperature phases.

activated MA motions along the C_3 and C_4 rotational axes play an indirect but important role in the electron−vibrational interaction, as established by the machine learning analysis.[127]

Besides the organic component, the Pb−I inorganic lattice is also strongly affected by thermal fluctuations in different phases. Importantly, since the fundamental band gap is determined by Pb and I atoms in $MAPbI_3$, the temperature-dependent distortions may exert strong influence on electron−hole interactions. Distributions of Pb−I bond lengths and I−Pb−I angles in the different structures are shown in Figure 2. Both the bond lengths and angles are strongly influenced by phase and temperature. For the four investigated systems, the calculated average Pb−I bond length and I−Pb−I angle values are 3.185, 3.248, 3.236, and 3.279 Å and 173.15, 168.09, 167.69, and 159.89° for Ortho-162 K, Tetra-162 K, Tetra-315 K, and Cubic-315 K, respectively, in agreement with the previously reported values of 3.10−3.30 Å and 152−175°.[121,128,129] The bond length and angle distributions become wider at the higher temperature, as expected. Interestingly, considering a phase pair at a particular phase transitions temperature, the higher-temperature phase exhibits wider distributions than the lower-temperature phase. Since this difference is observed at the same temperature for each phase pair, the higher-temperature phases are more intrinsically disordered than the lower-temperature phases. The disorder influences localization of electrons and holes, and their nonradiative recombination. The maxima of the distributions and the corresponding average values change systematically from phase to phase. The I−Pb−I angles decrease and the Pb−I distances increase from orthorhombic to tetragonal to cubic phase. Deformation of the $[PbI_6]^{4-}$ octahedra grows with temperature, and the Pb−I bonding weakens. The changes in the Pb−I interatomic interactions, caused by the phase transitions and temperature, influence electron−vibrational interactions and electron−hole recombination dynamics.

Additional information about the thermal atomic fluctuations is provided by the canonically averaged standard deviations of the positions for each type of atoms, $\sigma_i = \sqrt{\langle (\underset{r_i}{\rightarrow} - \langle \underset{r_i}{\rightarrow} \rangle)^2 \rangle}$. Here, $\underset{r_i}{\rightarrow}$ represents the location of atom i along the adiabatic MD trajectories, and the angular bracket stands for canonical averaging. The MA, Pb, and I species are considered separately (Table 1). The values

Table 1. Standard Deviations (Å) in the Positions of MA, Pb, and I Atoms in the Ortho-162 K, Tetra-162 K, Tetra-315 K, and Cubic-315 K $MAPbI_3$ Systems

	MA	Pb	I
Ortho-162 K	0.587	0.224	0.305
Tetra-162 K	0.628	0.232	0.321
Tetra-315 K	0.659	0.306	0.427
Cubic-315 K	0.739	0.389	0.484

increase with temperature and are larger for the higher-temperature phase: Ortho-162 K < Tetra-162 K < Tetra-315 K < Cubic-315 K, providing further evidence on the growing structural disorder due to thermal response and phase transition. Larger standard deviations indicate stronger atomic fluctuations. One expects that larger atomic fluctuations favor stronger NA coupling, which is proportional to the atomic velocity,[76] and accelerate vibrationally induced loss of electronic coherence.[84] Stronger NA coupling and faster decoherence have opposite effects on the charge carrier lifetime. Generally, stronger NA coupling speeds up the charge recombination, while faster decoherence slows it down.[76,130] The competition between these two factors governs the quantum dynamics and excited-state lifetimes. However, the NA coupling, reported in Table 2, is determined not only by the atomic velocity but also by overlap of the initial and final states,[76,130] which is analyzed below.

3.2. Electronic Properties. The projected density of states (PDOS) of the four investigated systems can be found in Figure S1. The PDOS are canonically averaged for each phase and temperature. The VBM is dominated by the antibonding

https://doi.org/10.1021/jacs.2c08627
J. Am. Chem. Soc. 2022, 144, 19137−19149

Table 2. Band Gap, Average Absolute NA Coupling, Pure-Dephasing Time, Nonradiative Electron−Hole Recombination Time, and Radiative Lifetime for the VBM−CBM Transition in the Ortho-162 K, Tetra-162 K, Tetra-315 K, and Cubic-315 K $MAPbI_3$ Systems

	band gap (eV)	NA coupling (meV)	dephasing (fs)	nonradiative recombination (ns)	radiative recombination (ns)
Ortho-162 K	1.65[44]	1.33	24.7	1.19	1.47
Tetra-162 K	1.68[131]	1.10	18.2	1.34	2.23
Tetra-315 K	1.68[131]	0.93	14.1	2.47	3.03
Cubic-315 K	1.55[132]	0.74	7.8	5.62	7.22

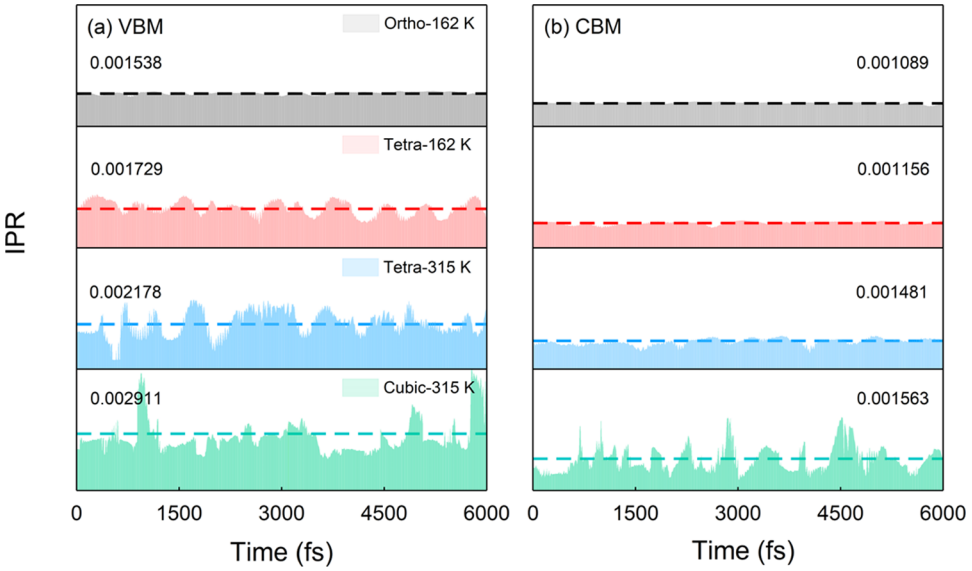

Figure 3. Evolution of the inverse participation ratio (IPR) of (a) VBM and (b) CBM in the Ortho-162 K, Tetra-162 K, Tetra-315 K, and Cubic-315 K $MAPbI_3$ systems. Larger IRP indicates more localization. The *y*-axis scale is the same in all cases. Atomic fluctuations grow with increasing temperature (Figure 2), and the charges become more localized.

interaction between I-5p and Pb-6s atomic orbitals. The CBM is predominantly composed of interacting Pb-6p and I-5p orbitals, with the Pb-6p orbitals contributing most. The organic MA cations do not affect the band edges directly, as the orbitals from C, N, and H are either far above or below the CBM and VBM. MA and other A-site cations contribute to electron−hole and electron−vibrational interactions indirectly through electrostatic interactions and by steric perturbations to the inorganic lattice.[127,133,134] The NA coupling responsible for the nonradiative electron−hole recombination is mainly created by the Pb and I atoms, because the recombination takes place between the CBM and the VBM. There is a mild band gap opening with increasing temperature. The canonically averaged direct band gaps follow the order: Ortho-162 K (1.61 eV) < Tetra-162 K (1.65 eV) < Tetra-315 K (1.68 eV) < Cubic-315 K (1.76 eV), in agreement with the previous DFT calculations.[37,38,135,136] The trend in the band gaps is explained by the lattice distortion. On moving from Ortho-162 K to Tetra-162 K to Tetra-315 K to Cubic-315 K, there is a gradual decrease in the average I−Pb−I bond angle from 173.15 to 168.10° to 167.69 to 159.90°, respectively. The distortion of the inorganic lattice diminishes overlap of the Pb and I atomic orbitals. This decreases the antibonding interaction between the Pb-6p and I-5p orbitals, lowers the VBM, and increases the band gap. The calculated band gaps differ slightly from the experimental values: 1.65 eV for the orthorhombic phase, 1.68 eV for the tetragonal phase, and 1.55 eV for the cubic phase.[44,131,132,137] The charge carrier recombination depends on the band gap; however, the band gap variations with temperature and phase are small, and therefore, the band gap influence on the charge carrier lifetime is not significant.

The nonradiative recombination of charge carriers is strongly influenced by the NA coupling, which is a product of the atomic velocity and the electronic matrix element,[76,130] $\langle \phi_{CBM} | \nabla_R | \phi_{VBM} \rangle$. The velocity is determined by the kinetic energy that is proportional to temperature. The matrix element shows how electronic wave functions depend on atomic displacements. It requires that the wave functions of the initial and final states are localized within the same spatial area, and this property can be characterized by an overlap of the corresponding charge densities defined as squares of the wave functions. Examples of typical VBM and CBM charge densities are shown in Figure S2. In the low-temperature Ortho-162 K system, the conduction band electrons are mainly distributed on Pb atoms, and the valence band holes on both I and Pb atoms, in agreement with the PDOS analysis (Figure S1). For the Tetra-162 K system at the same temperature, holes are getting localized slightly due to the symmetry transformation and additional mild distortions, while electrons remain delocalized. As a result, the NAC is reduced by 17% compared to the Ortho-162 K system (Table 2), 1.10 and 1.33 meV for Tetra-162 K and Ortho-162 K, respectively. Upon heating to 315 K, the electrons and holes become more spatially separated due to significant thermal distortions, facilitating exciton dissociation and formation of polarons, as suggested by both experiments and simulations.[44,45,51,52] The larger degree of fluctuations in the I−Pb−I lattice in the cubic phase makes the charge carriers more localized relatively to the tetragonal

https://doi.org/10.1021/jacs.2c08627
J. Am. Chem. Soc. 2022, 144, 19137−19149

phase at the same temperature. The charge separation reduces the NA coupling further, by 30 and 44% relative to Ortho-162 K; 0.93 and 0.74 meV for Tetra-315 K and Cubic-315 K, respectively. The decreased overlap of electron and hole reduces the NA coupling and slows down the nonradiative electron−hole recombination in the higher-temperature phases.

To quantify the temperature-dependent charge localization of the key states, we computed the evolution of inverse participation ratio (IPR).[138,139] The IPR of a particular KS orbital can be defined as

$$\mathrm{IPR} = N \cdot \frac{\sum k_i^4}{\left(\sum k_i^2\right)^2}$$

$$\mathrm{IPR} \in (0, 1]$$

where N is the number of grid points, and k_i is the charge density within the volume corresponding to grid point i. The IPR value varies from 0 to 1, characterizing the degree of orbital localization, where "1" describes the situation in which the charge is localized entirely on a single site. Therefore, the larger is the IPR, the more localized is the charge density.

Figure 3 presents the IPR for the VBM and CBM orbitals along the 6 ps MD trajectories for each system, with the horizontal lines indicating the averaged values. The y-axis scale is the same in all panels. The canonically averaged IPR values are larger for the VBM than the CBM, indicating more significant localization, as exemplified by the charge density distributions in Figure S2. This observation can be rationalized partially by the fact that electrons are supported by Pb 6p atomic orbitals, while holes are localized primarily on I 5p atomic orbitals and secondarily on Pb 6s atomic orbitals. The iodines that make the primary contribution to the VBM are nonmetals that prefer more directional bonding and lead to higher charge localization, compared to the Pb metals atoms. Metal atoms maintain bonding upon distortion more easily than nonmetals, cf. covalent vs metallic bonding. Similar observations have been made in semiconductor quantum dots[140,141] and 2D perovskites.[94] The IPR values of both electron and hole increase as the temperature grows, indicating higher localization at higher temperatures. The amplitude of the IPR fluctuations increases with temperature as well, manifesting increased dynamic disorder at higher temperatures and in the higher-temperature phases. The phase and temperature-dependent localization of both electrons and holes has a strong influence on the NA coupling and charge carrier lifetimes. The charge localization analysis leads one to expect that higher-temperature phases should exhibit longer carrier lifetimes and reduced charge transport. An optimal device performance depends on a balance between these two factors. Therefore, the performance can be tuned by phase, temperature, and device architecture, e.g., thickness of the light-harvesting layer.

Next, we analyze the overlap of electron and hole charge densities.[66] Figure 4 displays the evolution of the overlap along the MD trajectories in the four systems. Thermal fluctuations induce structural disorder that tends to localize the electron and hole in different parts of the simulation cell. Note that the overlap of the charge densities, including overlap of the charge density with itself, cannot be properly normalized, while the charge densities themselves are normalized since they are squares of wave functions. Therefore, the absolute scale on the

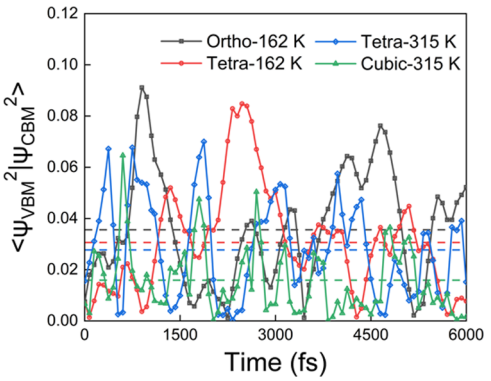

Figure 4. Evolution of overlap of the VBM and CBM charge densities along the MD trajectories in the Ortho-162 K, Tetra-162 K, Tetra-315 K, and Cubic-315 K $MAPbI_3$ systems. Electrons and holes become more separated at higher temperatures, and their overlap decreases, as demonstrated by the dashed lines showing the average overlaps. Notably, the electron−hole overlap fluctuates significantly and reaches zero even in the relatively small simulation cells used here. Considering the same temperature, the overlap is smaller for the cubic than tetragonal phase, and the tetragonal than orthorhombic phase.

y-axis should not be given a particular meaning. The electron−hole overlap fluctuates significantly during the simulation and often approaches zero, indicating that even in these relatively small simulation cells, compared to experimental systems, electrons and holes are able to separate efficiently. The overlap value decreases with increasing temperature: Ortho-162 K (3.58×10^{-2}) > Tetra-162 K (3.08×10^{-2}) > Tetra-315 K (2.82×10^{-2}) > Cubic-315 K (1.56×10^{-2}). This trend further explains why the charge carrier lifetime increases with temperature and for higher-temperature phases. A smaller electron−hole overlap correlates with a weaker NA coupling, and a longer electron−hole recombination process (Table 2).

3.3. Electron−Vibrational Interactions. Electron−vibrational interactions initiate inelastic and elastic electron−phonon scattering events, both of which influence the nonradiative electron−hole recombination. Inelastic scattering dissipates the electronic energy to phonons, while elastic scattering destroys superposition formed between the initial and final electronic states via the NA coupling, giving rise to quantum decoherence. In general, the electrons are excited to energies that are much higher than the thermal energy, both relative to the ground state and to the lowest-energy VBM−CBM excitation, while phonons are initially thermalized. On average, the energy flows from electrons to phonons; however, at any particular instance, there is a nonzero probability, included in the simulation, that the energy can flow back from phonons to electrons. Decoherence is closely related to pure-dephasing in the optical response theory.[83,84,130] It is typical that rapid decoherence delays quantum dynamics. Quantum transitions can even stop if the decoherence time is infinitesimal, manifested by the quantum Zeno effect.[79,83]

For the purpose of identifying the phonon modes participating in the nonradiative electron−hole recombination dynamics, we computed spectral densities by performing Fourier transforms (FTs) of the autocorrelation functions (ACFs) of the phonon-induced fluctuations of the energy gap. We also computed FT of the difference between the IPRs of the CBM and the VBM, and FT of the electron−hole charge density overlap. These spectral densities, shown in Figure 5,

https://doi.org/10.1021/jacs.2c08627
J. Am. Chem. Soc. 2022, 144, 19137−19149

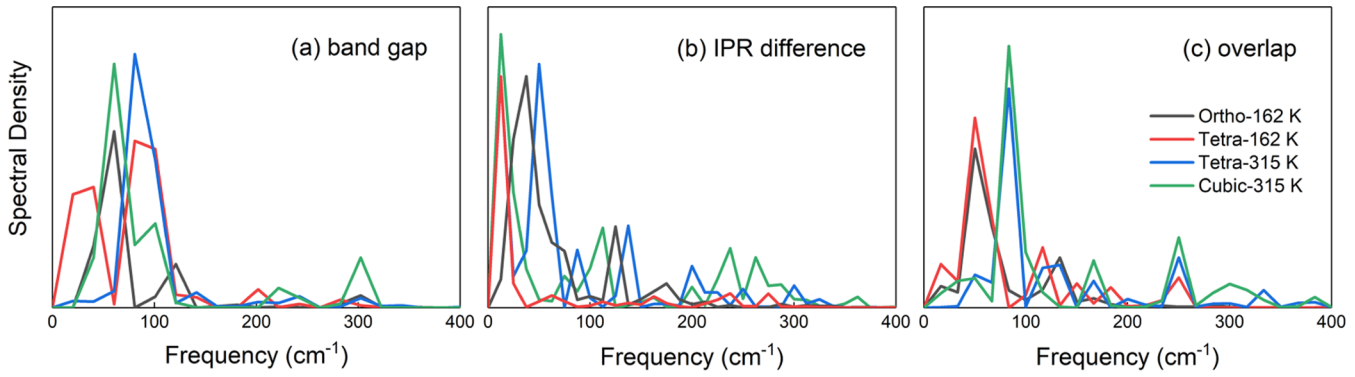

Figure 5. Spectral densities obtained by FTs of the autocorrelation functions of (a) VBM−CBM band gap fluctuations, (b) IPR difference, and (c) electron−hole charge density overlap for the Ortho-162 K, Tetra-162 K, Tetra-315 K, and Cubic-315 K $MAPbI_3$ systems. The charge−phonon coupling responsible for the nonradiative electron−hole recombination is driven primarily by low-frequency modes. The higher-frequency modes are most active in the cubic phase that exhibits the largest charge localization (Figure 3) and the smallest electron−hole overlap (Figure 4).

are dominated by low frequencies. Slow vibrations with frequencies lower than 100 cm^{-1} play a leading role in creating the NA coupling, accelerating the loss of coherence, and driving the electron−hole recombination dynamics. Notable signals are seen up to 300 cm^{-1}. The IPR difference shows the strongest signals above 100 cm^{-1}, indicating that charge localization is more sensitive to motions of the MA cations than charge overlap and NA coupling.

The peaks in the influence spectra (Figure 5) can be assigned to the following vibrations, based on the spectral measurements by Giustino et al.[142,143] The peak at 33 cm^{-1} is attributed to the distortion of the PbI_6 octahedra, and its frequency is slightly underestimated due to neglect of the spin−orbit interaction.[144] The major signal around 62−70 cm^{-1} corresponds to the I−Pb−I bending.[144] The Pb−I bond stretching signal is at 94 cm^{-1}.[144] Because the band-edge states are supported by the inorganic lattice, these modes play the most important role in the excited-state dynamics of electrons and holes near the band edge. The modes in the 120−180 cm^{-1} range are the Raman active librations of the fast and light organic MA cations.[144] The peaks around and above 200 cm^{-1} are associated with the C−N torsion of the MA cations.[142] Although the MA cations do not contribute to the electron and hole wave functions, they influence the charges via long-range electrostatic interactions, as well as by perturbing the inorganic Pb−I lattice sterically. As temperature increases, the intensities of the peaks in the influence spectra grow due to increased amplitude of vibrations, and new signals appear at higher frequencies because of growing anharmonicity that relaxes electron−vibrational coupling selection rules. As a result of increased fluctuations and anharmonicity,[84] the decoherence/pure-dephasing process accelerates at higher temperatures (Table 2).

Decoherence is an important factor for charge recombination. Caused by elastic electron−vibrational scattering, it destroys coherences between the initial and final states during the electronic transition, and thereby, influences the nonradiative relaxation. The decoherence time is estimated as the pure-dephasing time of the optical response theory.[83,84] Under the second-order cumulant approximation, the pure-dephasing function, $D_{ij}(t) = \exp\left(-\frac{1}{\hbar^2}\int_0^t dt' \int_0^{t'} dt'' \, C_{ij}(t'')\right)$, is determined by the unnormalized ACF (un-ACF), $C_{ij}(t) = \langle \delta E_{ij}(t')\delta E_{ij}(t - t')\rangle_{t'}$, of the fluctuation, $\delta E_{ij}(t)$, of the band gap from its canonically averaged value. The pure-dephasing time is controlled by the initial value and decay of the un-ACF. The larger the initial value and the faster the decay, the shorter the coherence time.[84]

The pure-dephasing functions and un-ACFs for the CBM−VBM transitions are shown in Figure 6. Fitting the data to a

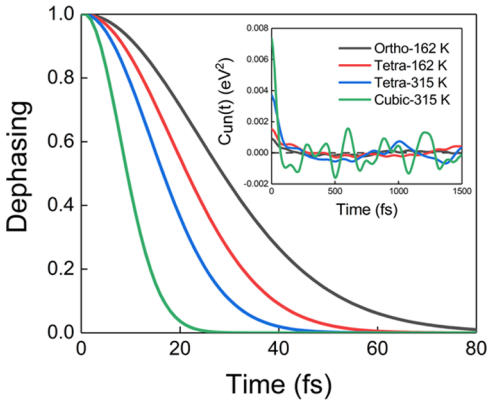

Figure 6. Pure-dephasing functions for the CBM−VBM transition in the Ortho-162 K, Tetra-162 K, Tetra-315 K, and Cubic-315 K $MAPbI_3$ systems. The inset shows the unnormalized autocorrelation functions (un-ACFs) of the CBM−VBM band gaps. The un-ACF initial value gives the square of the band gap fluctuations, and larger phonon-driven band gap fluctuation leads to faster coherence loss.

Gaussian, $\exp[-0.5(t/\tau)^2]$, gives the pure-dephasing times, τ, reported in Table 2. The pure-dephasing times are on the order of 10 fs and decrease with increasing temperature, from 24.7 to 18.2 fs to 14.1 to 7.8 fs for Ortho-162 K to Tetra-162 K to Tetra-315 K to Cubic-315 K, respectively. Considering the phase pairs at the phase-transition temperatures, the higher-temperature phases exhibit faster decoherence due to increased electronic disorder, as characterized by the IPR (Figure 3). As presented in the inset of Figure 6, the un-ACFs decay on similar timescales for the investigated systems, and therefore, the pure-dephasing rates are primarily determined by the un-ACF initial values, which equal to the square of the energy gap fluctuations.[84] At the higher temperature, the Cubic-315 K system exhibits a larger un-ACF initial value than the Tetra-315 K system, due to the larger atomic fluctuations (Table 1, Figure 1b). Similarly, the Tetra-162 K phase exhibits larger atomic fluctuations than the Ortho-162 K phase at a lower temperatures. Since rapid loss of quantum coherence tends to

https://doi.org/10.1021/jacs.2c08627
J. Am. Chem. Soc. 2022, 144, 19137−19149

suppress quantum dynamics,[79] the short decoherence times favor extended charge carrier lifetimes in $MAPbI_3$ at the higher temperature (Table 2), contributing to its overall high efficiency.

The calculations are performed in the regime in which only one electron and one hole are present in the simulation. At the same time, the volume of the simulation cell is relatively small, 7652 $Å^3$ for the orthogonal phase, 8083 $Å^3$ for the tetrahedral phase, and 7963 $Å^3$ for the cubic phase, due to computational limitations. Therefore, the carrier density is high, about 1.25×10^{-4} $Å^{-3}$ = 1.25×10^{20} cm^{-3}. However, because there are no additional carriers beside the recombining electron and hole, the energy released during the nonradiative recombination is deposited into phonons, as expected for low carrier densities encountered in solar cell applications. The model used in the current work most closely mimics solar cell operating conditions.

The evolution of the population of the first excited state, corresponding to the VBM-to-CBM excitation, characterizes the nonradiative electron−hole recombination across the fundamental band gap (Figure 7). Fitting the data to the exponential decay, $P(t) = \exp(-t/\tau)$, gives the electron−hole recombination timescales, τ, reported in Table 2. The NAMD simulations show that the nonradiative electron−hole recombination process slows down with increasing temperature and for the higher-temperature phase at the phase-transition temperature. The calculated timescales are on the order of several nanoseconds, which is consistent with the spectroscopy measurements and other calculations.[43,60−62,97,145] Note that the NAMD calculations assume that the electron and hole have already approached each other. Charge diffusion across large distances is not included in the ab initio quantum dynamics simulations.

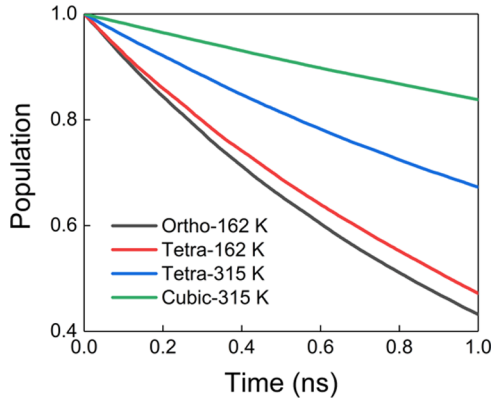

Figure 7. Nonradiative electron−hole recombination dynamics in the Ortho-162 K, Tetra-162 K, Tetra-315 K, and Cubic-315 K $MAPbI_3$ systems. The recombination slows down with increasing temperature due to enhanced charge localization (Figure 3) and decreased electron−hole overlap (Figure 4). These factors also explain the difference in the recombination times for different phases at the same temperature.

Reduced charge and energy losses, associated with the slower nonradiative electron−hole recombination, favor improved photovoltaic performance. The carrier lifetime increases with increasing temperature and for the higher-temperature phase. The nonradiative excited-state lifetimes calculated for the Ortho-162 K, Tetra-162 K, Tetra-315 K, and Cubic-315 K systems are 1.19, 1.34, 2.47, and 5.62 ns, respectively (Table 2). In comparison, the canonically averaged radiative lifetimes, estimated according to the Einstein coefficient of spontaneous emission by averaging over the first 2 ps of the 6 ps trajectories, are 1.47, 2.23, 3.03, and 7.22 ns. The radiative and nonradiative decay rates are comparable, indicating that light emission constitutes a major channel. The distributions of the radiative decay times, shown in Figure S3, are broad, indicating that thermal fluctuations of metal halide perovskites have a strong influence on both nonradiative and radiative decay channels.

The trend of the nonradiative electron−hole recombination times can be rationalized by considering the band gap, NA coupling, and pure-dephasing time, which enter the quantum dynamics simulations. Typically, greater band gap, smaller NA coupling, and faster pure-dephasing lead to longer recombination. As summarized in Table 2, although the band gap of the high-temperature cubic-phase system decreases by about 0.1 eV compared to that of the other two phases, the small gap difference results in only slight acceleration of the electron−hole recombination. Compared to the Ortho-162 K system, both the change in the lattice symmetry and activation of the C_4 rotation of the MA cations contribute to structural disorder that increases charge separation and atomic fluctuations in the Tetra-162 K system. The NA coupling declines by 17% and the pure-dephasing time falls by 26% for the Tetra-162 K system relative to the Ortho-162 K system. Considering the phase transition at 315 K, the differences in the thermal fluctuations and structural disorder between the Tetra-315 K and Cubic-315 K systems, and the higher temperature overall, lead to reduction of the NA coupling by 30 and 44% and the pure-dephasing time by 43 and 68%, respectively, relative to the Ortho-162 K system. The smaller NA coupling and shorter decoherence, due to increased structural disorder, play more important roles than the slight decrease in the band gap, making the Cubic-315 K system exhibit the longest charge carrier lifetime. The above detailed atomistic analysis clarifies the critical factors influencing the temperature-dependent excited-state lifetimes in HOIPs.

4. DISCUSSION AND CONCLUSIONS

We have investigated systematically the temperature-dependent nonradiative electron−hole recombination process in different phases of the methylammonium lead halide perovskite, by performing NAMD simulations combined with real-time TDDFT. The study has established the atomistic mechanism for the reduced charge recombination observed in experiments with increasing temperature and upon the phase transitions, providing a fundamental understanding of device performance under thermal influence. Many of the findings cannot be deduced just from experimental data.

The calculations show that the interaction between the inorganic and organic components depends strongly on the phase. The perovskite geometric construction is relatively ordered up to 162 K in the low-temperature orthorhombic phase. The charge carriers are delocalized, overlap well, interact strongly, and recombine efficiently. The change in the structural symmetry to the tetragonal phase causes mild distortions and allows stronger atomic fluctuations, inducing partial charge localization. As a result, the electrons and holes overlap less and live longer. As the material is heated to 315 K, thermal fluctuations increase significantly, the inorganic lattice becomes more distorted, and the organic cations rotate nearly freely. Strong structural disorder is introduced, facilitating

https://doi.org/10.1021/jacs.2c08627
J. Am. Chem. Soc. 2022, 144, 19137−19149

charge localization and exciton dissociation. The disorder is more significant in the higher-temperature cubic phase than the lower-temperature tetragonal phase, at the same temperature.

The inelastic and elastic electron−vibrational interactions exhibit opposite dependence on both temperature and phase. On the one hand, thermal disorder brings charge localization, reduces electron−hole overlap, and decreases the NA coupling responsible for energy dissipation by inelastic scattering. On the other hand, enhanced thermal atomic fluctuations increase anharmonicity and activate more phonon modes, favoring faster elastic scattering and coherence loss. The reduced NA coupling and shortened coherence time favor longer charge carrier lifetimes at higher temperatures, rationalizing the experimental observations.

The current work focused on pristine $MAPbI_3$, while defects play important roles in most semiconductors. HOIPs are remarkably defect-tolerant, and there is strong evidence, both experimental and theoretical, that defects in HOIPs behave differently from defects in more traditional semiconductors, such as Si and TiO_2. HOIPs are soft and adjust and heal defects well. The soft structure of HOIPs allows defect energy levels to fluctuate significantly. Deep levels can become shallow, and trapped charges escape into bands. Structural deformations induced by thermal fluctuations and phase transitions are on the same order as structural deformations induced by defects, and for this reason, thermal disorder plays a very important role.

The growth of the charge carrier lifetimes with increasing temperature and upon transformation to the higher-temperature phases is particularly favorable for applications since solar cells and optoelectronic devices heat up under operating conditions. The phenomenon is quite unique to metal halide perovskites and is not observed in traditional inorganic semiconductors. The longer carrier lifetimes arise from stronger charge localization, which can be detrimental to charge transport. The opposite trends in the charge lifetime and transport with temperature explain the contradictory experimental data on the temperature dependence of the device performance, which is governed by the charge diffusion length. Which factor wins depends on device architecture, material morphology, etc. The two factors, carrier lifetime and carrier transport, can be optimized to achieve the best performance.

The ab initio quantum dynamics simulations reported here rationalize the contradictory experimental observations and emphasize the strong influence of structural disorder and charge localization on the excited-state lifetimes in different $MAPbI_3$ phases. The simulations show that the structural disorder arising from the phase transitions is as important as the disorder arising from heating of a single phase. The atomistic insights into the perovskite properties provide guidance for controlling charge carrier dynamics in metal halide perovskites and related materials for optoelectronic applications.

■ ASSOCIATED CONTENT

Supporting Information

The Supporting Information is available free of charge at https://pubs.acs.org/doi/10.1021/jacs.2c08627.

Canonically averaged projected densities of states, representative charge densities of the band-edge states, canonical distributions of radiative lifetimes, and lattice parameters of the three phases (PDF)

■ AUTHOR INFORMATION

Corresponding Author

Run Long − *Key Laboratory of Theoretical & Computational Photochemistry of Ministry of Education, College of Chemistry, Beijing Normal University, Beijing 100875, People's Republic of China;* orcid.org/0000-0003-3912-8899; Email: runlong@bnu.edu.cn

Authors

Ran Shi − *Key Laboratory of Theoretical & Computational Photochemistry of Ministry of Education, College of Chemistry, Beijing Normal University, Beijing 100875, People's Republic of China*

Qiu Fang − *Key Laboratory of Theoretical & Computational Photochemistry of Ministry of Education, College of Chemistry, Beijing Normal University, Beijing 100875, People's Republic of China*

Andrey S. Vasenko − *HSE University, 101000 Moscow, Russia;* orcid.org/0000-0002-2978-8650

Wei-Hai Fang − *Key Laboratory of Theoretical & Computational Photochemistry of Ministry of Education, College of Chemistry, Beijing Normal University, Beijing 100875, People's Republic of China;* orcid.org/0000-0002-1668-465X

Oleg V. Prezhdo − *Departments of Chemistry, and Physics and Astronomy, University of Southern California, Los Angeles, California 90089, United States;* orcid.org/0000-0002-5140-7500

Complete contact information is available at: https://pubs.acs.org/10.1021/jacs.2c08627

Notes

The authors declare no competing financial interest.

■ ACKNOWLEDGMENTS

This work was supported by the Beijing Natural Science Foundation (grant no. 2212031) and the National Natural Science Foundation of China (grant nos. 21973006 and 21520102005). R.L. acknowledges the Recruitment Program of Global Youth Experts of China and the Beijing Normal University Startup. A.S.V. acknowledges support from the Mirror Laboratories Project and the Basic Research Program of the HSE University. O.V.P. acknowledges support from the U.S. National Science Foundation (grant no. CHE-2154367).

■ REFERENCES

(1) Prasanna, R.; Gold-Parker, A.; Leijtens, T.; Conings, B.; Babayigit, A.; Boyen, H.-G.; Toney, M. F.; McGehee, M. D. Band Gap Tuning via Lattice Contraction and Octahedral Tilting in Perovskite Materials for Photovoltaics. *J. Am. Chem. Soc.* **2017**, *139*, 11117−11124.

(2) Pellet, N.; Gao, P.; Gregori, G.; Yang, T.-Y.; Nazeeruddin, M. K.; Maier, J.; Graetzel, M. Mixed-Organic-Cation Perovskite Photovoltaics for Enhanced Solar-Light Harvesting. *Angew. Chem., Int. Ed.* **2014**, *53*, 3151−3157.

(3) Meggiolaro, D.; Motti, S. G.; Mosconi, E.; Barker, A. J.; Ball, J.; Perini, C. A. R.; Deschler, F.; Petrozza, A.; De Angelis, F. Iodine Chemistry Determines the Defect Tolerance of Lead-Halide Perovskites. *Energy Environ. Sci.* **2018**, *11*, 702−713.

(4) Lian, Z.; Yan, Q.; Gao, T.; Ding, J.; Lv, Q.; Ning, C.; Li, Q.; Sun, J.-l. Perovskite $CH_3NH_3PbI_3$(Cl) Single Crystals: Rapid Solution

Growth, Unparalleled Crystalline Quality, and Low Trap Density toward 10^8 cm^{-3}. *J. Am. Chem. Soc.* **2016**, *138*, 9409−9412.
(5) Liao, W.; Zhao, D.; Yu, Y.; Shrestha, N.; Ghimire, K.; Grice, C. R.; Wang, C.; Xiao, Y.; Cimaroli, A. J.; Ellingson, R. J.; Podraza, N. J.; Zhu, K.; Xiong, R.-G.; Yan, Y. Fabrication of Efficient Low-Bandgap Perovskite Solar Cells by Combining Formamidinium Tin Iodide with Methylammonium Lead Iodide. *J. Am. Chem. Soc.* **2016**, *138*, 12360−12363.
(6) Shi, D.; Adinolfi, V.; Comin, R.; Yuan, M.; Alarousu, E.; Buin, A.; Chen, Y.; Hoogland, S.; Rothenberger, A.; Katsiev, K.; Losovyj, Y.; Zhang, X.; Dowben, P. A.; Mohammed, O. F.; Sargent, E. H.; Bakr, O. M. Low Trap-State Density and Long Carrier Diffusion in Organolead Trihalide Perovskite Single Crystals. *Science* **2015**, *347*, 519−522.
(7) Ma, L.; Hao, F.; Stoumpos, C. C.; Phelan, B. T.; Wasielewski, M. R.; Kanatzidis, M. G. Carrier Diffusion Lengths of over 500 nm in Lead-Free Perovskite $CH_3NH_3SnI_3$ Films. *J. Am. Chem. Soc.* **2016**, *138*, 14750−14755.
(8) D'innocenzo, V.; Grancini, G.; Alcocer, M. J.; Kandada, A. R. S.; Stranks, S. D.; Lee, M. M.; Lanzani, G.; Snaith, H. J.; Petrozza, A. Excitons versus Free Charges in Organo-Lead Tri-Halide Perovskites. *Nat. Commun.* **2014**, *5*, No. 3586.
(9) Wehrenfennig, C.; Eperon, G. E.; Johnston, M. B.; Snaith, H. J.; Herz, L. M. High Charge Carrier Mobilities and Lifetimes in Organolead Trihalide Perovskites. *Adv. Mater.* **2014**, *26*, 1584−1589.
(10) Cao, F.; Meng, L.; Wang, M.; Tian, W.; Li, L. Gradient Energy Band Driven High-Performance Self-Powered Perovskite/CdS Photodetector. *Adv. Mater.* **2019**, *31*, No. 1806725.
(11) Shoaib, M.; Zhang, X.; Wang, X.; Zhou, H.; Xu, T.; Wang, X.; Hu, X.; Liu, H.; Fan, X.; Zheng, W.; Yang, T.; Yang, S.; Zhang, Q.; Zhu, X.; Sun, L.; Pan, A. Directional Growth of Ultralong $CsPbBr_3$ Perovskite Nanowires for High-Performance Photodetectors. *J. Am. Chem. Soc.* **2017**, *139*, 15592−15595.
(12) Liu, Y.; Dong, Y.; Zhu, T.; Ma, D.; Proppe, A.; Chen, B.; Zheng, C.; Hou, Y.; Lee, S.; Sun, B.; Jung, E. H.; Yuan, F.; Wang, Y.-k.; Sagar, L. K.; Hoogland, S.; de Arquer, F. P. G.; Choi, M.-J.; Singh, K.; Kelley, S. O.; Voznyy, O.; Lu, Z.-H.; Sargent, E. H. Bright and Stable Light-Emitting Diodes Based on Perovskite Quantum Dots in Perovskite Matrix. *J. Am. Chem. Soc.* **2021**, *143*, 15606−15615.
(13) Wei, Z.; Xing, J. The Rise of Perovskite Light-Emitting Diodes. *J. Phys. Chem. Lett.* **2019**, *10*, 3035−3042.
(14) Wu, Y.; Li, J.; Xu, J.; Du, Y.; Huang, L.; Ni, J.; Cai, H.; Zhang, J. Organic-Inorganic Hybrid $CH_3NH_3PbI_3$ Perovskite Materials as Channels in Thin-Film Field-Effect Transistors. *RSC Adv.* **2016**, *6*, 16243−16249.
(15) Li, Y. J.; Lv, Y.; Zou, C.-L.; Zhang, W.; Yao, J.; Zhao, Y. S. Output Coupling of Perovskite Lasers from Embedded Nanoscale Plasmonic Waveguides. *J. Am. Chem. Soc.* **2016**, *138*, 2122−2125.
(16) Huang, W.; Sadhu, S.; Ptasinska, S. Heat- and Gas-Induced Transformation in $CH_3NH_3PbI_3$ Perovskites and Its Effect on the Efficiency of Solar Cells. *Chem. Mater.* **2017**, *29*, 8478−8485.
(17) Prochowicz, D.; Runjhun, R.; Tavakoli, M. M.; Yadav, P.; Saski, M.; Alanazi, A. Q.; Kubicki, D. J.; Kaszkur, Z.; Zakeeruddin, S. M.; Lewinski, J.; Gratzel, M. Engineering of Perovskite Materials Based on Formamidinium and Cesium Hybridization for High-Efficiency Solar Cells. *Chem. Mater.* **2019**, *31*, 1620−1627.
(18) Kojima, A.; Teshima, K.; Shirai, Y.; Miyasaka, T. Organometal Halide Perovskites as Visible-Light Sensitizers for Photovoltaic Cells. *J. Am. Chem. Soc.* **2009**, *131*, 6050−6051.
(19) Kim, M.; Jeong, J.; Lu, H.; Lee, T. K.; Eickemeyer, F. T.; Liu, Y.; Choi, I. W.; Choi, S. J.; Jo, Y.; Kim, H.-B.; Mo, S.-I.; Kim, Y.-K.; Lee, H.; An, N. G.; Cho, S.; Tress, W. R.; Zakeeruddin, S. M.; Hagfeldt, A.; Kim, J. Y.; Grätzel, M.; Kim, D. S. Conformal Quantum Dot-SnO_2 Layers as Electron Transporters for Efficient Perovskite Solar Cells. *Science* **2022**, *375*, 302−306.
(20) Yang, J.; Siempelkamp, B. D.; Liu, D.; Kelly, T. L. Investigation of $CH_3NH_3PbI_3$ Degradation Rates and Mechanisms in Controlled Hmidity Evironments Uing in Situ Techniques. *ACS Nano* **2015**, *9*, 1955−1963.
(21) He, J.; Fang, W.-H.; Long, R.; Prezhdo, O. V. Superoxide/Peroxide Chemistry Extends Charge Carriers' Lifetime but Undermines Chemical Stability of $CH_3NH_3PbI_3$ Exposed to Oxygen: Time-Domain AB Initio Analysis. *J. Am. Chem. Soc.* **2019**, *141*, 5798−5807.
(22) Lang, F.; Shargaieva, O.; Brus, V. V.; Neitzert, H. C.; Rappich, J.; Nickel, N. H. Influence of Radiation on the Properties and the Stability of Hybrid Perovskites. *Adv. Mater.* **2018**, *30*, No. 1702905.
(23) Juarez-Perez, E. J.; Ono, L. K.; Maeda, M.; Jiang, Y.; Hawash, Z.; Qi, Y. Photodecomposition and Thermal Decomposition in Methylammonium Halide Lead Perovskites and Inferred Design Principles to Increase Photovoltaic Device Stability. *J. Mater. Chem. A* **2018**, *6*, 9604−9612.
(24) Aranda, C. A.; Caliò, L.; Salado, M. Toward Commercialization of Stable Devices: An Overview on Encapsulation of Hybrid Organic-Inorganic Perovskite Solar Cells. *Crystals* **2021**, *11*, No. 519.
(25) Lv, Y.; Zhang, H.; Liu, R.; Sun, Y.; Huang, W. Composite Encapsulation Enabled Superior Comprehensive Stability of Perovskite Solar Cells. *ACS Appl. Mater. Interfaces* **2020**, *12*, 27277−27285.
(26) Skoplaki, E.; Boudouvis, A.; Palyvos, J. A Simple Correlation for the Operating Temperature of Photovoltaic Modules of Arbitrary Mounting. *Sol. Energy Mater. Sol. Cells* **2008**, *92*, 1393−1402.
(27) Skoplaki, E.; Palyvos, J. A. On the Temperature Dependence of Photovoltaic Module Electrical Performance: A Review of Efficiency/Power Correlations. *Sol. Energy* **2009**, *83*, 614−624.
(28) He, J.; Fang, W.-h.; Long, R. Unravelling the Effects of Oxidation State of Interstitial Iodine and Oxygen Passivation on Charge Trapping and Recombination in $CH_3NH_3PbI_3$ Perovskite: a Time-Domain AB Initio Study. *Chem. Sci.* **2019**, *10*, 10079−10088.
(29) Whalley, L. D.; van Gerwen, P.; Frost, J. M.; Kim, S.; Hood, S. N.; Walsh, A. Giant Huang-Rhys Factor for Electron Capture by the Iodine Intersitial in Perovskite Solar Cells. *J. Am. Chem. Soc.* **2021**, *143*, 9123−9128.
(30) Hoque, M. N. F.; Islam, N.; Li, Z.; Ren, G.; Zhu, K.; Fan, Z. Ionic and Optical Properties of Methylammonium Lead Iodide Perovskite across the Tetragonal-Cubic Structural Phase Transition. *ChemSusChem* **2016**, *9*, 2692−2698.
(31) Whitfield, P. S.; Herron, N.; Guise, W.; Page, K.; Cheng, Y.; Milas, I.; Crawford, M. Structures, Phase Transitions and Tricritical Behavior of the Hybrid Perovskite Methylammonium Lead Iodide. *Sci. Rep.* **2016**, *6*, No. 35685.
(32) Ho, J.; Easton, C. J.; Coote, M. L. The Distal Effect of Electron-Withdrawing Groups and Hydrogen Bonding on the Stability of Peptide Enolates. *J. Am. Chem. Soc.* **2010**, *132*, 5515−5521.
(33) Ong, K. P.; Goh, T. W.; Xu, Q.; Huan, A. Mechanical Origin of the Structural Phase Transition in Methylammonium Lead Iodide $CH_3NH_3PbI_3$. *J. Phys. Chem. Lett.* **2015**, *6*, 681−685.
(34) Herz, L. M. Charge-Carrier Dynamics in Organic-Inorganic Metal Halide Perovskites. *Annu. Rev. Phys. Chem.* **2016**, *67*, 65−89.
(35) Dittrich, T.; Awino, C.; Prajongtat, P.; Rech, B.; Lux-Steiner, M. C. Temperature Dependence of the Band Gap of $CH_3NH_3PbI_3$ Stabilized with PMMA: a Modulated Surface Photovoltage study. *J. Phys. Chem. C* **2015**, *119*, 23968−23972.
(36) Quarti, C.; Mosconi, E.; Ball, J. M.; D'Innocenzo, V.; Tao, C.; Pathak, S.; Snaith, H. J.; Petrozza, A.; De Angelis, F. Structural and Optical Properties of Methylammonium Lead Iodide across the Tetragonal to Cubic Phase Transition: Implications for Perovskite Solar Cells. *Energy Environ. Sci.* **2016**, *9*, 155−163.
(37) Foley, B. J.; Marlowe, D. L.; Sun, K.; Saidi, W. A.; Scudiero, L.; Gupta, M. C.; Choi, J. J. Temperature Dependent Energy Levels of Methylammonium Lead Iodide Perovskite. *Appl. Phys. Lett.* **2015**, *106*, No. 243904.
(38) Saidi, W. A.; Poncé, S.; Monserrat, B. Temperature Dependence of the Energy Levels of Methylammonium Lead Iodide Perovskite from First-Principles. *J. Phys. Chem. Lett.* **2016**, *7*, 5247−5252.
(39) O'Donnell, K. P.; Chen, X. Temperature Dependence of Semiconductor Band Gaps. *Appl. Phys. Lett.* **1991**, *58*, 2924−2926.
(40) Savenije, T. J.; Ponseca, C. S., Jr.; Kunneman, L.; Abdellah, M.; Zheng, K.; Tian, Y.; Zhu, Q.; Canton, S. E.; Scheblykin, I. G.;

https://doi.org/10.1021/jacs.2c08627
J. Am. Chem. Soc. 2022, 144, 19137−19149

Pullerits, T.; et al. Thermally Activated Exciton Dissociation and Recombination Control the Carrier Dynamics in Organometal Halide Perovskite. *J. Phys. Chem. Lett.* **2014**, *5*, 2189−2194.
(41) Mayers, M. Z.; Tan, L. Z.; Egger, D. A.; Rappe, A. M.; Reichman, D. R. How Lattice and Charge Fluctuations Control Carrier Dynamics in Halide Perovskites. *Nano Lett.* **2018**, *18*, 8041−8046.
(42) Yi, H. T.; Wu, X.; Zhu, X.; Podzorov, V. Intrinsic Charge Transport across Phase Transitions in Hybrid Organo-Inorganic Perovskites. *Adv. Mater.* **2016**, *28*, 6509−6514.
(43) Greenland, C.; Shnier, A.; Rajendran, S. K.; Smith, J. A.; Game, O. S.; Wamwangi, D.; Turnbull, G. A.; Samuel, I. D.; Billing, D. G.; Lidzey, D. G. Correlating Phase Behavior with Photophysical Properties in Mixed-Cation Mixed-Halide Perovskite Thin Films. *Adv. Energy Mater.* **2020**, *10*, No. 1901350.
(44) Phuong, L. Q.; Yamada, Y.; Nagai, M.; Maruyama, N.; Wakamiya, A.; Kanemitsu, Y. Free Carriers versus Excitons in $CH_3NH_3PbI_3$ Perovskite Thin Films at Low Temperatures: Charge Transfer from the Orthorhombic Phase to the Tetragonal Phase. *J. Phys. Chem. Lett.* **2016**, *7*, 2316−2321.
(45) Kong, W.; Ye, Z.; Qi, Z.; Zhang, B.; Wang, M.; Rahimi-Iman, A.; Wu, H. Characterization of an Abnormal Photoluminescence Behavior upon Crystal-Phase Transition of Perovskite $CH_3NH_3PbI_3$. *Phys. Chem. Chem. Phys.* **2015**, *17*, 16405−16411.
(46) Even, J.; Pedesseau, L.; Katan, C. Analysis of Multivalley and Multibandgap Absorption and Enhancement of Free Carriers Related to Exciton Screening in Hybrid Perovskites. *J. Phys. Chem. C* **2014**, *118*, 11566−11572.
(47) Zhang, Z. S.; Long, R.; Tokina, M. V.; Prezhdo, O. V. Interplay between Localized and Free Charge Carriers Can Explain Hot Fluorescence in the $CH_3NH_3PbBr_3$ Perovskite: Time-Domain Ab Initio Analysis. *J. Am. Chem. Soc.* **2017**, *139*, 17327−17333.
(48) Mladenović, M.; Vukmirović, N. Effects of Thermal Disorder on the Electronic Structure of Halide Perovskites: Insights from MD Simulations. *Phys. Chem. Chem. Phys.* **2018**, *20*, 25693−25700.
(49) Zhu, H.; Trinh, M. T.; Wang, J.; Fu, Y.; Joshi, P. P.; Miyata, K.; Jin, S.; Zhu, X. Y. Organic Cations Might not be Essential to the Remarkable Properties of Band Edge Carriers in Lead Halide Perovskites. *Adv. Mater.* **2017**, *29*, No. 1603072.
(50) Zhu, H.; Miyata, K.; Fu, Y.; Wang, J.; Joshi, P. P.; Niesner, D.; Williams, K. W.; Jin, S.; Zhu, X. Y. Screening in Crystalline Liquids Protects Energetic Carriers in Hybrid Perovskites. *Science* **2016**, *353*, 1409−1413.
(51) Nandi, P.; Giri, C.; Swain, D.; Manju, U.; Mahanti, S. D.; Topwal, D. Temperature Dependent Photoinduced Reversible Phase Separation in Mixed-Halide Perovskite. *ACS Appl. Energy Mater.* **2018**, *1*, 3807−3814.
(52) Zhu, X.-Y.; Podzorov, V. Charge Carriers in Hybrid Organic-Inorganic Lead Halide Perovskites Might be Protected as Large Polarons. *J. Phys. Chem. Lett.* **2015**, *6*, 4758−4761.
(53) Cui, X.; Yuan, S.; Zhang, H.; Zhang, X.; Wang, P.; Tu, L.; Sun, Z.; Wang, J.; Zhan, Y.; Zheng, L. Temperature-Dependent Electronic Properties of Inorganic-Organic Hybrid Halide Perovskite ($CH_3NH_3PbBr_3$) Single Crystal. *Appl. Phys. Lett.* **2017**, *111*, No. 233302.
(54) Ambrosio, F.; Mosconi, E.; Alasmari, A. A.; Alasmary, F. A.; Meggiolaro, D.; De Angelis, F. Formation of Color Centers in Lead Iodide Perovskites: Self-Trapping and Defects in the Bulk and Surfaces. *Chem. Mater.* **2020**, *32*, 6916−6924.
(55) Tong, C. J.; Cai, X. Y.; Zhu, A. Y.; Liu, L. M.; Prezhdo, O. V. How Hole Injection Accelerates Both Ion Migration and Nonradiative Recombination in Metal Halide Perovskites. *J. Am. Chem. Soc.* **2022**, *144*, 6604−6612.
(56) Li, W.; She, Y. L.; Vasenko, A. S.; Prezhdo, O. V. Ab initio nonadiabatic molecular dynamics of charge carriers in metal halide perovskites. *Nanoscale* **2021**, *13*, 10239−10265.
(57) Diroll, B. T. Temperature-Dependent Intraband Relaxation of Hybrid Perovskites. *J. Phys. Chem. Lett.* **2019**, *10*, 5623−5628.
(58) Madjet, M. E.; Berdiyorov, G. R.; El-Mellouhi, F.; Alharbi, F. H.; Akimov, A. V.; Kais, S. Cation Effect on Hot Carrier Cooling in Halide Perovskite Materials. *J. Phys. Chem. Lett.* **2017**, *8*, 4439−4445.
(59) Chen, J.; Messing, M. E.; Zheng, K.; Pullerits, T. Cation-Dependent Hot Carrier Cooling in Halide Perovskite Nanocrystals. *J. Am. Chem. Soc.* **2019**, *141*, 3532−3540.
(60) Trimpl, M. J.; Wright, A. D.; Schutt, K.; Buizza, L. R.; Wang, Z.; Johnston, M. B.; Snaith, H. J.; Müller-Buschbaum, P.; Herz, L. M. Charge-Carrier Trapping and Radiative Recombination in Metal Halide Perovskite Semiconductors. *Adv. Funct. Mater.* **2020**, *30*, No. 2004312.
(61) Wehrenfennig, C.; Liu, M.; Snaith, H. J.; Johnston, M. B.; Herz, L. M. Charge Carrier Recombination Channels in the Low-Temperature Phase of Organic-Inorganic Lead Halide Perovskite Thin Films. *APL Mater.* **2014**, *2*, No. 081513.
(62) Milot, R. L.; Eperon, G. E.; Snaith, H. J.; Johnston, M. B.; Herz, L. M. Temperature-Dependent Charge-Carrier Dynamics in $CH_3NH_3PbI_3$ Perovskite Thin Films. *Adv. Funct. Mater.* **2015**, *25*, 6218−6227.
(63) Johnston, M. B.; Herz, L. M. Hybrid Perovskites for Photovoltaics: Charge-Carrier Recombination, Diffusion, and Radiative Efficiencies. *Acc. Chem. Res.* **2016**, *49*, 146−154.
(64) Gélvez-Rueda, M. C.; Cao, D. H.; Patwardhan, S.; Renaud, N.; Stoumpos, C. C.; Schatz, G. C.; Hupp, J. T.; Farha, O. K.; Savenije, T. J.; Kanatzidis, M. G.; Grozema, F. C. Effect of Cation Rotation on Charge Dynamics in Hybrid Lead Halide Perovskites. *J. Phys. Chem. C* **2016**, *120*, 16577−16585.
(65) Munson, K. T.; Kennehan, E. R.; Doucette, G. S.; Asbury, J. B. Dynamic Disorder Dominates Delocalization, Transport, and Recombination in Halide Perovskites. *Chem* **2018**, *4*, 2826−2843.
(66) Li, W.; Tang, J.; Casanova, D.; Prezhdo, O. V. Time-Domain Ab Initio Analysis Rationalizes the Unusual Temperature Dependence of Charge Carrier Relaxation in Lead Halide Perovskite. *ACS Energy Lett.* **2018**, *3*, 2713−2720.
(67) Wang, Y.; Long, R. Anomalous Temperature-Dependent Charge Recombination in $CH_3NH_3PbI_3$ Perovskite: Key Roles of Charge Localization and Thermal Effect. *ACS Appl. Mater. Interfaces* **2019**, *11*, 32069−32075.
(68) Li, W.; Vasenko, A. S.; Tang, J. F.; Prezhdo, O. V. Anharmonicity Extends Carrier Lifetimes in Lead Halide Perovskites at Elevated Temperatures. *J. Phys. Chem. Lett.* **2019**, *10*, 6219−6226.
(69) Kohn, W.; Sham, L. J. Self-Consistent Equations Including Exchange and Correlation Effects. *Phys. Rev.* **1965**, *140*, A1133−A1138.
(70) Craig, C. F.; Duncan, W. R.; Prezhdo, O. V. Trajectory Surface Hopping in the Time-Dependent Kohn-Sham Approach for Electron-Nuclear Dynamics. *Phys. Rev. Lett.* **2005**, *95*, No. 163001.
(71) Mai, S. B.; Gonzalez, L. Molecular Photochemistry: Recent Developments in Theory. *Angew. Chem., Int. Ed.* **2020**, *59*, 16832−16846.
(72) Jankowska, J.; Sobolewski, A. L. Modern Theoretical Approaches to Modeling the Excited-State Intramolecular Proton Transfer: An Overview. *Molecules* **2021**, *26*, No. 5140.
(73) Nottoli, M.; Cupellini, L.; Lipparini, F.; Granucci, G.; Mennucci, B. Multiscale Models for Light-Driven Processes. *Annu. Rev. Phys. Chem.* **2021**, *72*, 489−513.
(74) You, P. W.; Chen, D. Q.; Lian, C.; Zhang, C.; Meng, S. First-Principles Dynamics of Photoexcited Molecules and Materials towards a Quantum Description. *WIREs Comput. Mol. Sci.* **2021**, *11*, No. e1492.
(75) Zheng, Z. F.; Jiang, X.; Chu, W. B.; Zhang, L. L.; Guo, H. L.; Zhao, C. Y.; Wang, Y. N.; Wang, A. L.; Zheng, Q. J.; Zhao, J. Investigation of Ab Initio Nonadiabatic Molecular Dynamics of Excited Carriers in Condensed Matter Systems. *Acta Phys. Sin.* **2021**, *70*, No. 177101.
(76) Prezhdo, O. V. Modeling Non-adiabatic Dynamics in Nanoscale and Condensed Matter Systems. *Acc. Chem. Res.* **2021**, *54*, 4239−4249.

https://doi.org/10.1021/jacs.2c08627
J. Am. Chem. Soc. 2022, 144, 19137−19149

(77) Giannini, S.; Blumberger, J. Charge Transport in Organic Semiconductors: The Perspective from Nonadiabatic Molecular Dynamics. *Acc. Chem. Res.* **2022**, *55*, 819−830.
(78) Prezhdo, O. V. Quantized Hamilton Dynamics. *Theor. Chem. Acc.* **2006**, *116*, 206−218.
(79) Kilina, S. V.; Neukirch, A. J.; Habenicht, B. F.; Kilin, D. S.; Prezhdo, O. V. Quantum Zeno Effect Rationalizes the Phonon Bottleneck in Semiconductor Quantum Dots. *Phys. Rev. Lett.* **2013**, *110*, No. 180404.
(80) Jaeger, H. M.; Fischer, S.; Prezhdo, O. V. Decoherence-Induced Surface Hopping. *J. Chem. Phys.* **2012**, *137*, No. 22A545.
(81) Akimov, A. V.; Prezhdo, O. V. The PYXAID Program for Non-Adiabatic Molecular Dynamics in Condensed Matter Systems. *J. Chem. Theory Comput.* **2013**, *9*, 4959−4972.
(82) Akimov, A. V.; Prezhdo, O. V. Advanced Capabilities of the PYXAID Program: Integration Schemes, Decoherence Effects, Multiexcitonic States, and Field-Matter Interaction. *J. Chem. Theory Comput.* **2014**, *10*, 789−804.
(83) Mukamel, S.*Principles of Nonlinear Optical Spectroscopy*; Oxford University Press: New York, 1995.
(84) Akimov, A. V.; Prezhdo, O. V. Persistent Electronic Coherence Despite Rapid Loss of Electron-Nuclear Correlation. *J. Phys. Chem. Lett.* **2013**, *4*, 3857−3864.
(85) Kamisaka, H.; Kilina, S. V.; Yamashita, K.; Prezhdo, O. V. Ab Initio Study of Temperature and Pressure Dependence of Energy and Phonon-Induced Dephasing of Electronic Excitations in CdSe and PbSe Quantum Dots. *J. Phys. Chem. C* **2008**, *112*, 7800−7808.
(86) Zhang, Z. S.; Fang, W. H.; Tokina, M. V.; Long, R.; Prezhdo, O. V. Rapid Decoherence Suppresses Charge Recombination in Multi-Layer 2D Halide Perovskites: Time-Domain Ab Initio Analysis. *Nano Lett.* **2018**, *18*, 2459−2466.
(87) Wei, Y.; Long, R. Grain Boundaries are Benign and Suppress Nonradiatie Electron−Hole Recombination in Monolayer Black Phosphorus: A Time-Domain AB Initio Study. *J. Phys. Chem. Lett.* **2018**, *9*, 3856−3862.
(88) Zhang, L. L.; Vasenko, A. S.; Zhao, J.; Prezhdo, O. V. Mono-Elemental Properties of 2D Black Phosphorus Ensure Extended Charge Carrier Lifetimes under Oxidation: Time-Domain Ab Initio Analysis. *J. Phys. Chem. Lett.* **2019**, *10*, 1083−1091.
(89) Yang, Y.; Fang, W.-H.; Benderskii, A.; Long, R.; Prezhdo, O. V. Strain Controls Charge Carrier Lifetimes in Monolayer WSe_2: Ab Initio Time Domain Analysis. *J. Phys. Chem. Lett.* **2019**, *10*, 7732−7739.
(90) Yaffe, O.; Guo, Y.; Tan, L. Z.; Egger, D. A.; Hull, T.; Stoumpos, C. C.; Zheng, F.; Heinz, T. F.; Kronik, L.; Kanatzidis, M. G.; Owen, J. S.; Rappe, A. M.; Pimenta, M. A.; Brus, L. E. Local Polar Fluctuations in Lead Halide Perovskite Crystals. *Phys. Rev. Lett.* **2017**, *118*, No. 13600.
(91) Wang, X.; Long, R. Oxidation Notably Accelerates Non-radiative Electron-Hole Recombination in MoS_2 by Different Mechanisms: Time-Domain Ab Initio Analysis. *J. Phys. Chem. Lett.* **2020**, *11*, 4086−4092.
(92) Li, L. Q.; Long, R.; Prezhdo, O. V. Why Chemical Vapor Deposition Grown MoS_2 Samples Outperform Physical Vapor Deposition Samples: Time-Domain ab Initio Analysis. *Nano Lett.* **2018**, *18*, 4008−4014.
(93) Zhu, Y. H.; Fang, W. H.; Rubio, A.; Long, R.; Prezhdo, O. V. The Twist Angle has Weak Influence on Charge Separation and Strong Influence on Recombination in the MoS_2/WS_2 Bilayer: Ab Initio Quantum Dynamics. *J. Mater. Chem. A* **2022**, *10*, 8324−8333.
(94) Zhang, Z.; Fang, W.-H.; Long, R.; Prezhdo, O. V. Exciton Dissociation and Suppressed Charge Recombination at 2D Perovskite Edges: Key Roles of Unsaturated Halide Bonds and Thermal Disorder. *J. Am. Chem. Soc.* **2019**, *141*, 15557−15566.
(95) Shi, R.; Zhang, Z.; Fang, W.-H.; Long, R. Charge Localization Control of Electron-Hole Recombination in Multilayer Two-Dimensional Dion-Jacobson Hybrid Perovskites. *J. Mater. Chem. A* **2020**, *8*, 9168−9176.
(96) Zhang, Z.; Long, R. Doping-Induced Rapid Decoherence Suppresses Charge Recombination in Mono/Divalent Cations Mixed Perovskite from Nonadiabatic Molecular Dynamics Simulation. *J. Phys. Chem. Lett.* **2019**, *10*, 3433−3439.
(97) Shi, R.; Long, R. Hole Localization Inhibits Charge Recombination in Tin-Lead Mixed Perovskites: Time-Domain ab Initio Analysis. *J. Phys. Chem. Lett.* **2019**, *10*, 6604−6612.
(98) Shi, R.; Fang, W.-H.; Vasenko, A. S.; Long, R.; Prezhdo, O. V. Efficient Passivation of DY Center in $CH_3NH_3PbBr_3$ by Chlorine: Quantum Molecular Dynamics. *Nano Res.* **2022**, 2112−2122.
(99) Wu, Y. F.; Chu, W. B.; Vasenko, A. S.; Prezhdo, O. V. Common Defects Accelerate Charge Carrier Recombination in $CsSnI_3$ without Creating Mid-Gap States. *J. Phys. Chem. Lett.* **2021**, *12*, 8699−8705.
(100) Zhao, X.; Long, R. Isotopic Exchange Extends Charge Carrier Lifetime in Metal Lead Perovskites by Quantum Dynamics Simulations. *J. Phys. Chem. Lett.* **2020**, *11*, 10298−10305.
(101) Qiao, L.; Fang, W. H.; Long, R.; Prezhdo, O. V. Atomic Model for Alkali Metal Passivation of Point Defects at Perovskite Grain Boundaries. *ACS Energy Lett.* **2020**, *5*, 3813−3820.
(102) Zhao, X.; Long, R. Benign Effects of Twin Boundaries on Charge Carrier Lifetime in Metal Halide Perovskites by a Time-Domain Study. *J. Phys. Chem. Lett.* **2021**, *12*, 8575−8582.
(103) Shi, R.; Vasenko, A. S.; Long, R.; Prezhdo, O. V. Edge Influence on Charge Carrier Localization and Lifetime in $CH_3NH_3PbBr_3$ Perovskite: Ab Initio Quantum Dynamics Simulation. *J. Phys. Chem. Lett.* **2020**, *11*, 9100−9109.
(104) Qiao, L.; Fang, W.-H.; Long, R. The Interplay Between Lead Vacancy and Water Rationalizes the Puzzle of Charge Carrier Lifetimes in $CH_3NH_3PbI_3$: Time-Domain Ab Initio Analysis. *Angew. Chem., Int. Ed.* **2020**, *59*, 2−9.
(105) Qiao, L.; Fang, W. H.; Prezhdo, O. V.; Long, R. Suppressing Oxygen-Induced Deterioration of Metal Halide Perovskites by Alkaline Earth Metal Doping: A Quantum Dynamics Study. *J. Am. Chem. Soc.* **2022**, *144*, 5543−5551.
(106) Qiao, L.; Fang, W.-H.; Long, R.; Prezhdo, O. V. Elimination of Charge Recombination Centers in Metal Halide Perovskites by Strain. *J. Am. Chem. Soc.* **2021**, *143*, 9982−9990.
(107) Qiao, L.; Fang, W. H.; Long, R.; Prezhdo, O. V. Photoinduced Dynamics of Charge Carriers in Metal Halide Perovskites from an Atomistic Perspective. *J. Phys. Chem. Lett.* **2020**, *11*, 7066−7082.
(108) Long, R.; Prezhdo, O. V. Asymmetry in the Electron and Hole Transfer at a Polymer-Carbon Nanotube Heterojunction. *Nano Lett.* **2014**, *14*, 3335−3341.
(109) Long, R.; English, N. J.; Prezhdo, O. V. Defects Are Needed for Fast Photo-Induced Electron Transfer from a Nanocrystal to a Molecule: Time-Domain Ab Initio Analysis. *J. Am. Chem. Soc.* **2013**, *135*, 18892−18900.
(110) Zhang, Z. S.; Liu, L. H.; Fang, W. H.; Long, R.; Tokina, M. V.; Prezhdo, O. V. Plasmon-Mediated Electron Injection from Au Nanorods into MoS_2: Traditional versus Photoexcitation Mechanism. *Chem* **2018**, *4*, 1112−1127.
(111) Agrawal, S.; Vasenko, A. S.; Trivedi, D. J.; Prezhdo, O. V. Charge Carrier Nonadiabatic Dynamics in Non-Metal Doped Graphitic Carbon Nitride. *J. Chem. Phys.* **2022**, *156*, No. 094702.
(112) Cheng, C.; Zhu, Y. H.; Fang, W. H.; Long, R.; Prezhdo, O. V. CO Adsorbate Promotes Polaron Photoactivity on the Reduced Rutile TiO_2(110) Surface. *JACS Au* **2022**, *2*, 234−245.
(113) Kresse, G.; Furthmüller, J. Efficient Iterative Schemes for AB Initio Total-Energy Calculations Using a Plane-Wave Basis Set. *Phys. Rev. B* **1996**, *54*, 11169−11186.
(114) Perdew, J. P.; Burke, K.; Ernzerhof, M. Generalized Gradient Approximation Made Simple. *Phys. Rev. Lett.* **1996**, *77*, 3865−3869.
(115) Blöchl, P. E. Projector Augmented-Wave Method. *Phys. Rev. B* **1994**, *50*, 17953.
(116) Grimme, S.; Antony, J.; Ehrlich, S.; Krieg, H.; Consistent, A. and Accurate AN Initio Parametrization of Density Functional Dispersion Correction (DFT-D) for the 94 Elements H-Pu. *J. Chem. Phys.* **2010**, *132*, No. 154104.

https://doi.org/10.1021/jacs.2c08627
J. Am. Chem. Soc. 2022, 144, 19137−19149

(117) Grimme, S.; Ehrlich, S.; Goerigk, L. Effect of the Damping Function in Dispersion Corrected Density Functional Theory. *J. Comput. Chem.* **2011**, *32*, 1456−1465.
(118) Chu, W. B.; Saidi, W. A.; Zhao, J.; Prezhdo, O. V. Soft Lattice and Defect Covalency Rationalize Tolerance of beta-$CsPbI_3$ Perovskite Solar Cells to Native Defects. *Angew. Chem., Int. Ed.* **2020**, *59*, 6435−6441.
(119) Chu, W. B.; Prezhdo, O. V. Concentric Approximation for Fast and Accurate Numerical Evaluation of Nonadiabatic Coupling with Projector Augmented-Wave Pseudopotentials. *J. Phys. Chem. Lett.* **2021**, *12*, 3082−3089.
(120) Brivio, F.; Frost, J. M.; Skelton, J. M.; Jackson, A. J.; Weber, O. J.; Weller, M. T.; Goni, A. R.; Leguy, A. M.; Barnes, P. R.; Walsh, A. Lattice Dynamics and Vibrational Spectra of the Orthorhombic, Tetragonal, and Cubic Phases of Methylammonium Lead Iodide. *Phys. Rev. B* **2015**, *92*, No. 144308.
(121) Thind, A. S.; Huang, X.; Sun, J.; Mishra, R. First-Principles Prediction of a Stable Hexagonal Phase of $CH_3NH_3PbI_3$. *Chem. Mater.* **2017**, *29*, 6003−6011.
(122) Quarti, C.; Mosconi, E.; De Angelis, F. Interplay of Orientational Order and Electronic Structure in Methylammonium Lead Iodide: Implications for Solar Cell Operation. *Chem. Mater.* **2014**, *26*, 6557−6569.
(123) Mattoni, A.; Filippetti, A.; Saba, M.; Delugas, P. Methylammonium Rotational Dynamics in Lead Halide Perovskite by Classical Molecular Dynamics: the Role of Temperature. *J. Phys. Chem. C* **2015**, *119*, 17421−17428.
(124) Rossi, D.; Pecchia, A.; der Maur, M. A.; Leonhard, T.; Röhm, H.; Hoffmann, M. J.; Colsmann, A.; Di Carlo, A. On the Importance of Ferroelectric Domains for the Performance of Perovskite Solar Cells. *Nano Energy* **2018**, *48*, 20−26.
(125) Li, Y.; Behtash, M.; Wong, J.; Yang, K. Enhancing Ferroelectric Dipole Ordering in Organic-Inorganic Hybrid Perovskite $CH_3NH_3PbI_3$: Strain and Doping Engineering. *J. Phys. Chem. C* **2018**, *122*, 177−184.
(126) Wang, C.; Liu, Y.; Liu, S. F.; Li, B.; Chen, Y. Giant Phonon Tuning Effect via Pressure-Manipulated Polar Rotation in Perovskite $MAPbI_3$. *J. Phys. Chem. Lett.* **2018**, *9*, 3029−3034.
(127) Zhou, G. Q.; Chu, W. B.; Prezhdo, O. V. Structural Deformation Controls Charge Losses in $MAPbI_3$: Unsupervised Machine Learning of Nonadiabatic Molecular Dynamics. *Acs Energy Lett.* **2020**, *5*, 1930−1938.
(128) Mosconi, E.; Azpiroz, J. M.; De Angelis, F. Ab Initio Molecular Dynamics Simulations of Methylammonium Lead Iodide Perovskite Degradation by Water. *Chem. Mater.* **2015**, *27*, 4885−4892.
(129) Lin, C.; Li, S.; Zhang, W.; Shao, C.; Yang, Z. Effect of Bromine Substitution on the Ion Migration and Optical Absorption in $MAPbI_3$ Perovskite Solar Cells: the First-Principles Study. *ACS Appl. Energy Mater.* **2018**, *1*, 1374−1380.
(130) Prezhdo, O. V.; Rossky, P. J. Evaluation of Quantum Transition Rates from Quantum-Classical Molecular Dynamics Simulations. *J. Chem. Phys.* **1997**, *107*, 5863−5878.
(131) Barker, A. J.; Sadhanala, A.; Deschler, F.; Gandini, M.; Senanayak, S. P.; Pearce, P. M.; Mosconi, E.; Pearson, A. J.; Wu, Y.; Srimath Kandada, A. R.; et al. Defect-Assisted Photoinduced Halide Segregation in Mixed-Halide Perovskite Thin Films. *ACS Energy Lett.* **2017**, *2*, 1416−1424.
(132) Hao, F.; Stoumpos, C. C.; Chang, R. P.; Kanatzidis, M. G. Anomalous Band Gap Behavior in Mixed Sn and Pb Perovskites Enables Broadening of Absorption Spectrum in Solar Cells. *J. Am. Chem. Soc.* **2014**, *136*, 8094−8099.
(133) Mangan, S. M.; Zhou, G. Q.; Chu, W. B.; Prezhdo, O. V. Dependence between Structural and Electronic Properties of $CsPbI_3$: Unsupervised Machine Learning of Nonadiabatic Molecular Dynamics. *J. Phys. Chem. Lett.* **2021**, *12*, 8672−8678.
(134) Liu, D. Y.; Perez, C. M.; Vasenko, A. S.; Prezhdo, O. V. Ag-Bi Charge Redistribution Creates Deep Traps in Defective $Cs_2AgBiBr_6$: Machine Learning Analysis of Density Functional Theory. *J. Phys. Chem. Lett.* **2022**, *13*, 3645−3651.
(135) Ali, I. O. A.; Joubert, D. P.; Suleiman, M. S. A Theoretical Investigation of Structural, Mechanical, Electronic and Thermoelectric Properties of Orthorhombic $CH_3NH_3PbI_3$. *Eur. Phys. J. B* **2018**, *91*, No. 8902.
(136) Saidi, W. A.; Kachmar, A. Effects of Electron−Phonon Coupling on Electronic Properties of Methylammonium Lead Iodide Perovskites. *J. Phys. Chem. Lett.* **2018**, *9*, 7090−7097.
(137) Zhong, M.; Zeng, W.; Tang, H.; Wang, L.-X.; Liu, F.-S.; Tang, B.; Liu, Q.-J. Band Structures, Effective Masses and Exciton Binding Energies of Perovskite Polymorphs of $CH_3NH_3PbI_3$. *Sol. Energy* **2019**, *190*, 617−621.
(138) Justo, J. F.; de Brito Mota, F.; Fazzio, A. First-Principles Investigation of a−SiN_x:H. *Phys. Rev. B* **2002**, *65*, No. 073202.
(139) Ashhab, S.; Voznyy, O.; Hoogland, S.; Sargent, E. H.; Madjet, M. E. Effect of Disorder on Transport Properties in a Tight-Binding Model for Lead Halide Perovskites. *Sci. Rep.* **2017**, *7*, No. 8902.
(140) Sowers, K. L.; Hou, Z.; Peterson, J. J.; Swartz, B.; Pal, S.; Prezhdo, O.; Krauss, T. D. Photophysical Properties of CdSe/CdS Core/Shell Quantum Dots with Tunable Surface Composition. *Chem. Phys.* **2016**, *471*, 24−31.
(141) Wei, H. H.-Y.; Evans, C. M.; Swartz, B. D.; Neukirch, A. J.; Young, J.; Prezhdo, O. V.; Krauss, T. D. Colloidal Semiconductor Quantum Dots with Tunable Surface Composition. *Nano Lett.* **2012**, *12*, 4465−4471.
(142) Pérez-Osorio, M. A.; Milot, R. L.; Filip, M. R.; Patel, J. B.; Herz, L. M.; Johnston, M. B.; Giustino, F. Vibrational Properties of the Organic−Inorganic Halide Perovskite $CH_3NH_3PbI_3$ from Theory and Experiment: Factor Group Analysis, First-Principles Calculations, and Low-Temperature Infrared Spectra. *J. Phys. Chem. C* **2015**, *119*, 25703−25718.
(143) Poncé, S.; Schlipf, M.; Giustino, F. Origin of Low Carrier Mobilities in Halide Perovskites. *ACS Energy Lett.* **2019**, *4*, 456−463.
(144) Quarti, C.; Grancini, G.; Mosconi, E.; Bruno, P.; Ball, J. M.; Lee, M. M.; Snaith, H. J.; Petrozza, A.; De Angelis, F. The Raman Spectrum of the $CH_3NH_3PbI_3$ Hybrid Perovskite: Interplay of Theory and Experiment. *J. Phys. Chem. Lett.* **2014**, *5*, 279−284.
(145) Klein, J. R.; Flender, O.; Scholz, M.; Oum, K.; Lenzer, T. Charge Carrier Dynamics of Methylammonium Lead Iodide: from PbI_2-Rich to Low-Dimensional Broadly Emitting Perovskites. *Phys. Chem. Chem. Phys.* **2016**, *18*, 10800−10808.

https://doi.org/10.1021/jacs.2c08627
J. Am. Chem. Soc. 2022, 144, 19137−19149